Journal of
Materials Chemistry A

Materials for energy and sustainability

Accepted Manuscript

This article can be cited before page numbers have been issued, to do this please use: K. Lee, Y. Ting, C. Chang, T. Lin, S. Chang, T. Hsueh, C. Lin and S. Lu, *J. Mater. Chem. A*, 2026, DOI: 10.1039/D6TA02888H.




ROYAL SOCIETY OF CHEMISTRY

rsc.li/materials-a

# Interfacial Electron Transfer-Driven Activity Enhancements of Carbide/Alloy Heterostructured Catalysts toward Water Electrolysis for High-Performance Anion Exchange Membrane Water Electrolysis

View Article Online
DOI: 10.1039/D6TA02888H

Kai-An Lee,[a] Yu-Chieh Ting, [a] Chiung-Wen Chang, [a] Tzu-Hsiang Lin, [a] Shao-I Chang, [a] Tsung-Wei Hsueh, [a] Chia-Hsien Lin,[a] Shih-Yuan Lu[a]*

[a] Department of Chemical Engineering, National Tsing Hua University, Hsinchu 300044, Taiwan
*Email: sylu@mx.nthu.edu.tw



## Abstract

Designing highly efficient and durable electrocatalysts remains a key challenge for practical alkaline water electrolysis. Here, rationally designed carbide/alloy heterostructured catalysts, $Mo_2C$/NiMo for hydrogen evolution reaction (HER) and $Mo_2C$/FeNiMo for oxygen evolution reaction (OER), were developed for activity enhancement driven by interfacial electron transfer to enable anion exchange membrane water electrolysis (AEMWE) of extraordinary performances. $Mo_2C$/NiMo and $Mo_2C$/FeNiMo achieved ultralow overpotentials of 169 and 303 mV, respectively at 500 mA $cm^{-2}$. The $Mo_2C$//NiMo@NF//PiperION//$Mo_2C$//FeNiMo@NF based AEMWE delivered an exceptionally high current density of 2.645 A $cm^{-2}$ at 2.0 V, along with an insignificant 2.0 % decay after 50 h of operation at a commercially relevant current density of 0.5 A $cm^{-2}$, underscoring its outstanding catalytic efficiency and durability. In the two carbide/alloy heterostructured catalysts, electron flows from the alloy domain to the carbide domain, triggering the interfacial synergy. The interfacial synergy promotes efficient coupling of water dissociation and $H_2$ desorption along the Volmer-Heyrovsky route to boost HER activities of $Mo_2C$/NiMo, and creates more electropositive Fe and Ni for favorable formation of active high-valent intermediates to realize high OER activities of $Mo_2C$/FeNiMo. This work highlights the great promise of carbide/alloy heterostructures as advanced electrocatalysts for scalable and efficient alkaline water electrolysis.

**Keywords:** heterostructured catalyst, carbide/alloy, interfacial electron transfer, water electrolysis, anion exchange membrane water electrolysis

## 1. Introduction

View Article Online
DOI: 10.1039/D6TA02888H

With the rise of global environmental awareness, achieving net-zero carbon emissions has become a core objective in global energy development. And development of clean energy alternatives to fossil fuels has become a critical issue [1]. Hydrogen has emerged as a key enabler of the on-going energy transition because of its high energy densities and carbon-free nature. Beyond serving as a clean fuel, hydrogen also plays a critical role in power generation, industrial energy supply, and high-value chemical feedstock [2]. Therefore, the development of sustainable and scalable hydrogen production technologies is of paramount importance for advancing green energy infrastructure. In this regard, electrocatalytic water splitting stands out as a promising green hydrogen production technology [3], and in particular anion exchange membrane water electrolysis (AEMWE) emerges as a favorable water-splitting technology [4, 5].

AEMWE integrates the advantages of both proton exchange membrane water electrolysis (PEMWE) and alkaline water electrolysis (AWE), enabling use of non-precious transition metal catalysts for cost-effective, efficient, and stable water electrolysis operations [6, 7]. Membrane electrode assembly (MEA), the core working unit of an AEMWE, is composed of two catalyst loaded electrodes, cathode and anode, and an anion exchange membrane (AEM) [8]. The catalysts loaded at the cathode and anode catalyze hydrogen evolution reaction (HER) and oxygen evolution reaction (OER), respectively, playing a decisive role in governing the overall efficiency of an AEMWE. Rational design of electrocatalysts specifically tailored for the two fundamental reactions of water electrolysis, HER and OER, in alkaline media is thus critical for prevailing of the AEMWE technology for green hydrogen production.

A wide variety of strategies for advancing catalyst performances have been proposed and explored, including nanostructure control, defect engineering, heteroatom doping, alloying, construction of heterostructures, etc. Heterostructured materials, in particular, have drawn increasing attentions in recent years as promising electrocatalysts for a wide range of electrochemical reactions, including HER, OER, oxygen reduction reaction, etc. [9, 10]. A heterostructure is generally defined as a composite material composed of two or more distinct solid-state phases that form well-defined heterointerfaces. Compared with their single-phase counterparts, heterostructured catalysts typically exhibit superior catalytic activities, which can be attributed to several advantages. First, the creation of heterostructures can substantially increase the density of accessible active sites. In addition, rationally designed nanostructured morphologies within heterostructures can further enhance structural robustness and durability during electrochemical operations [11]. In addition, the electronegativity difference between distinct components within a heterostructure often drives electron transfer across the interface. This interfacial electron redistribution can modulate the local electronic structure or even the overall band structure, thereby optimizing the adsorption energies of key intermediates and ultimately enhancing the catalytic activity [12]. Finally, the synergistic effect plays a pivotal role in the design of heterostructured catalysts. By integrating complementary

View Article Online
DOI: 10.1039/D6TA02888H

functionalities at the heterointerface, such effects not only introduce additional active sites for adsorption/desorption but also optimize the reaction pathways, thereby markedly enhancing the overall catalytic performance [13].

Transition metal carbides (TMCs) have garnered significant attentions as promising electrocatalysts because of their unique electronic structures, high electrical conductivities, and noble-metal-like catalytic properties [14]. The strong orbital hybridization between transition metals and carbon atoms can induce a downshift of the d-band center, thereby optimizing the metal-hydrogen binding energy. Such optimization promotes more favorable hydrogen adsorption–desorption kinetics, ultimately enhancing the catalytic performance toward HER [15, 16]. Furthermore, metal carbides can also function as an integral component of heterostructured materials, thereby imparting outstanding catalytic activities. For instance, Diao et al. employed a simple solid-state synthesis strategy to construct $W_2N$/WC heterostructured catalysts. Benefiting from the abundant heterointerfaces, $W_2N$/WC exhibited excellent electrocatalytic performances [17]. Zhao et al. reported a synergistic integration of $Mo_2C$ and $MoS_2$, forming a hybrid nanostructure of vertically aligned $MoS_2$/$Mo_2C$ nanosheets. In this architecture, the edges of the two-dimensional $MoS_2$ provided a favorable environment for the uniform dispersion of $Mo_2C$, thereby maximizing the exposure of active sites and consequently enhancing the overall catalytic performance [18]. Xu et al. manipulated the Mo-H binding energy by incorporating transition metals (Ni, Co, or Fe) into $Mo_2C$. This modulation originates from the interfacial interactions between the transition metals and $Mo_2C$ [19]. In addition to assessing catalytic activities through electrochemical performance measurements, further insights into the intrinsic properties of the catalysts can be obtained by density functional theory (DFT) calculations. Yuan et al. designed an electrode composed of Mo-$Mo_2C$ on a Mo plate, and DFT results revealed that the incorporation of metallic Mo into the heterostructure optimizes the electronic structure of $Mo_2C$. This modification not only lowers the energy barrier for water dissociation but also tunes the hydrogen adsorption free energy, thereby contributing to the enhanced catalytic performance [20].

Based on the aforementioned studies, it is evident that transition metals can interact with metal carbides to enhance catalytic activities through formation of heterointerfaces and interfacial electron transfer. Building on this insight, we developed two distinct heterostructured electrocatalysts tailored for HER and OER, respectively. These catalysts, composed of $Mo_2C$ and transition metal alloys, leverage the synergy between the metal carbide and alloy phases to achieve superior water splitting performances. In this work, a simple and fast dip-roast-reduction process was developed to uniformly load carbide/alloy heterostructured catalysts onto nickel foam (NF) substrates. In terms of material design, $Mo_2C$/NiMo was prepared for HER, whereas $Mo_2C$/FeNiMo was designed for OER. For HER, $Mo_2C$/NiMo required overpotentials of only 37 and 169 mV to reach current densities of 10 and 500 mA $cm^{-2}$, respectively whereas $Mo_2C$/FeNiMo delivered the same current densities at overpotentials of only 218 and 303 mV,

respectively. When integrated as the cathode and anode in an AEMWE, these catalysts enabled a remarkably high current density of 2.645 A $cm^{-2}$ at 2.0 V, demonstrating exceptional catalytic efficiency. Furthermore, in-situ X-ray absorption spectroscopy (XAS) and in-situ Raman spectroscopy were conducted to probe the reaction mechanisms, offering mechanistic insights into the origin of the enhanced activity. Overall, the rational design of carbide/alloy heterostructured catalysts presented here demonstrates significant potentials for commercial scale AEMWE, providing a promising pathway toward sustainable green hydrogen production to help reach the net-zero carbon emission goal.

View Article Online
DOI: 10.1039/D6TA02888H



## 2. Experimental section

### 2.1. Chemicals

Iron(II) chloride tetrahydrate ($FeCl_2 \cdot 4H_2O$, 98.0%), platinum (20 wt% on carbon black), and iridium(IV) oxide ($IrO_2$, >99.99%) were purchased from Thermo Fisher Scientific. Molybdenum(Ⅴ) chloride ($MoCl_5$, >99.6%) and Nafion D-521 dispersion (5% w/w in water and 1-propanol) were purchased from Alfa Aesar. Nickel(II) chloride hexahydrate ($NiCl_2 \cdot 6H_2O$, 96.0%) was obtained from Showa Chemical Industry Co., Ltd. Carboxylic acid-modified carbon nanotubes (MCNT, AMC-C tube-010, >98.0%) were provided by Golden Innovation Business Co., Ltd. Anhydrous ethanol (99.5%) was obtained from Echo Chemical Co., Ltd. Potassium hydroxide (KOH, 85%) was purchased from Honeywell Research Chemicals. Nickel foam substrates (NF, 90 PPI with 1.7 mm in thickness and 95 PPI with 0.3 mm in thickness) were obtained from May Chun Co., Ltd. Anion exchange membrane (Versogen PiperION, 40 μm) was supplied by Fuel Cell Store.

### 2.2. Fabrications of $Mo_2C$/NiMo, $Mo_2C$/FeNiMo, $Mo_2C$, NiMo, and FeNiMo

$NiCl_2 \cdot 6H_2O$ (68.7 mM) and $MoCl_5$ (68.7 mM) were dissolved, together with 10.0 mg of MCNT dispersed, in 10 mL of EtOH under ultrasonication for at least 10 minutes to form the precursor dispersion, into which a piece of NF was dipped to be coated with a layer of the precursor dispersion for a subsequent roast process. The precursor dispersion enveloped NF (1.0 cm × 2.0 cm) (90 PPI, 1.7 mm in thickness) was placed 0.5 cm above the nozzle of a butane firing gas torch (Diarex Co., Ltd.) to combust the solvent, EtOH, to trigger the oxidation of $NiCl_2 \cdot 6H_2O$ and $MoCl_5$ to form intermediate precursors for Ni and Mo. The dip-and-roast process was repeated for 30 times. The intermediate precursor coated NF was then calcined in an atmosphere of 5 % $H_2$/Ar at 600 °C for 2 hours to afford the $Mo_2C$/NiMo heterostructured catalyst loaded NF, termed $Mo_2C$/NiMo@NF. The $Mo_2C$/NiMo loaded NF was cut into pieces of 0.5 cm × 0.5 cm in size for materials and electrochemical characterizations. The catalyst mass loading on NF was estimated as the weight difference between the pristine NF and the catalyst loaded NF, to be about 30 mg $cm^{-2}$. The preparation procedures for $Mo_2C$/FeNiMo, $Mo_2C$, NiMo, and FeNiMo were the same with those of

View Article Online
DOI: 10.1039/D6TA02888H



$Mo_2C$/NiMo, except for the formulas of the precursor dispersions. For $Mo_2C$/FeNiMo, the precursor dispersion was composed of $FeCl_2{\cdot}4H_2O$ (17.2 mM), $NiCl_2{\cdot}6H_2O$ (68.7 mM), $MoCl_5$ (68.7 mM), and 10.0 mg of MCNT. For $Mo_2C$, the precursor dispersion was composed of $MoCl_5$ (51.5 mM) and 20.0 mg of MCNT. For NiMo, the precursor solution was composed of $NiCl_2{\cdot}6H_2O$ (68.7 mM) and $MoCl_5$ (10.3 mM) without the presence of MCNT. For FeNiMo, the precursor solution contains $FeCl_2{\cdot}4H_2O$ (17.2 mM), $NiCl_2{\cdot}6H_2O$ (68.7 mM), and $MoCl_5$ (12.9 mM), without the presence of MCNT. For electrochemical characterizations of the AEMWE, thin NF substrates (2.3 cm × 2.3 cm, 95 PPI, 0.3 mm in thickness) were used for loading of the catalyst to reduce the overall resistance of the device. Furthermore, the catalyst mass loading was reduced to 15 mg $cm^{-2}$ for optimal electrochemical performances of the AEMWE. The catalyst loaded NF was cut into pieces of 2.0 cm × 2.0 cm in size for assembly of the AEMWE.

### 2.3. Fabrications of Pt/C and $IrO_2$ Electrodes

Benchmark noble metal based cathode and anode, Pt/C for HER and $IrO_2$ for OER, respectively were fabricated with a drop-casting method. Commercial $IrO_2$ (or Pt/C) powder of 10.0 mg was dispersed in a 2.0 mL mixture solution containing ethanol (1.9 mL) and Nafion solution (0.1 mL), with the Nafion solution serving as a binder. The resulting suspension underwent ultrasonication for at least 1 hour to achieve a homogeneous catalyst ink. Subsequently, 20 μL of the $IrO_2$ (or Pt/C) catalyst ink was drop-cast onto a 0.5 cm × 0.5 cm piece of NF (90 PPI, 1.7 mm in thickness), followed by drying in an oven at 60 °C for 10 minutes. This procedure was repeated 20 times to attain a catalyst loading of 30.0 mg $cm^{-2}$.

### 2.4. Pre-treatment of Anion Exchange Membrane

An anion exchange membrane was cut into pieces of 3.5 cm × 3.5 cm in size and immersed in 1.0 M KOH at room temperature for at least 24 hours to achieve complete conversion of carbonate to hydroxide form in the AEM.

### 2.5. Assembly of Anion Exchange Membrane Water Electrolyzer

The anion exchange membrane water electrolyzer (AEMWE) was composed of two stainless steel end plates, two gold-plated copper bipolar plates, two stainless steel flow fields, two PTFE gaskets, one $Mo_2C$/NiMo cathode (2 cm × 2 cm), one $Mo_2C$/FeNiMo anode (2 cm × 2 cm), and one activated AEM. The membrane electrode assembly (MEA) was fabricated by sandwiching the AEM between the $Mo_2C$/NiMo cathode and $Mo_2C$/FeNiMo anode, followed by pressing together the rest of the components inside out in the following order: gaskets, flow fields, bipolar plates, and end plates. The AEMWE was tightened using a digital torque wrench set at 1.2 N·m. A 1.0 M KOH electrolyte was fed to the anode side at a flow rate of 30 mL $min^{-1}$ for at least 10 hours to ensure complete membrane wetting prior to the measurements. The system temperature was controlled at 60 °C in operation.

### 2.6. Materials Characterizations

X-ray diffraction (XRD) patterns were recorded using a Bruker D8A25 diffractometer with Cu Kα radiation as the X-ray source. Elemental composition was determined with inductively coupled plasma optical emission spectroscopy (ICP-OES, Thermo Scientific iCAP 7200 Duo). Raman spectra were recorded using a Micro Raman Identify Dual system (PTT, MRID) with a 532 nm green laser as the light source. Sample morphology was examined with field-emission scanning electron microscopy (FE-SEM, HITACHI SU8010). Atomic structure and elemental distribution were characterized with high-resolution transmission electron microscopy (HRTEM, JEOL JEM-ARM200FTH), high-angle annular dark-field scanning transmission electron microscopy (HAADF-STEM), and energy dispersive X-ray spectroscopy (EDS). Surface oxidation states of the samples were probed with high-resolution X-ray photoelectron spectroscopy (HRXPS, ULVAC-PHI Quantera II) equipped with an Al X-ray source. X-ray absorption spectroscopy (XAS) measurements were conducted at the National Synchrotron Radiation Research Center (NSRRC), Taiwan. Ex-situ and in-situ XAS spectra of Fe, Ni, and Mo K-edges were collected at beamline TPS 44A1 in a transmission mode under operations in a quick-scanning transmission mode.

### 2.7. Electrochemical Characterizations

Electrochemical characterizations were conducted with a CHI6273E electrochemical workstation. The catalyst loaded NF serves as the working electrode (0.5 cm × 0.5 cm) with a blank NF (1 cm × 2 cm) and Hg/HgO (BAS Inc., RE-61AP) used as the counter and reference electrodes, respectively. The Hg/HgO reference electrode was pre-calibrated in 1.0 M KOH before use. Cyclic voltammetry (CV) was conducted for 30 cycles at 100 mV $s^{-1}$ within potential windows of 0 to -0.4 V (vs. RHE) and 1.0 to 1.5 V (vs. RHE) for HER and OER, respectively to stabilize the catalysts. Linear sweep voltammetry (LSV) was conducted at 1 mV $s^{-1}$ within the same potential windows, with a 90% iR-compensation applied. Electrochemical impedance spectroscopy (EIS) was conducted at -0.2 V (vs. RHE) and 1.58 V (vs. RHE) for HER and OER, respectively over the frequency range of 10 kHz to 0.01 Hz. Double-layer capacitance ($C_{dl}$) was estimated from CVs recorded within a non-Faradaic potential window of 50 mV in width at increasing scan rates from 10 to 50 mV $s^{-1}$ at an interval of 10 mV $s^{-1}$.

### 2.8. AEMWE Measurements

Electrochemical performances of AEMWEs were measured with a BioLogic HCP-803 potentiostat. CV was conducted within a voltage window of 1.2 to 1.8 V at 100 mV $s^{-1}$ for 10 cycles prior to LSV measurements. The LSV was conducted at 1 mV $s^{-1}$ from 1.2 to 2.0 V without application of iR-compensation. EIS was recorded at 1.8 V over a frequency range of 10 kHz to 0.1 Hz. Long-term stability was assessed at 0.5 A $cm^{-2}$ for 50 hours.

View Article Online
DOI: 10.1039/D6TA02888H

## 3. Result and Discussion

### 3.1. Materials characterizations

The catalysts were prepared with a simple dip-roast-reduction method. Briefly, precursors, including metal salts and MCNTs, are first loaded onto a NF substrate through a dip-and-roast process, followed by a thermal reduction treatment to afford the product catalysts (**Scheme S1**). In addition to the carbide/alloy heterostructured catalysts, $Mo_2C$/NiMo for HER and $Mo_2C$/FeNiMo for OER, corresponding single component control catalysts, including $Mo_2C$, NiMo, and FeNiMo, were also prepared for comparison. **Figure 1a** shows the XRD patterns of the five sample catalysts. Two characteristic sets of diffraction peaks are observed for the two heterostructured catalysts, one set (2θ of 34.6, 38.2, 39.6, 52.4, 61.8, 69.7, 74.9, and 75.6°) corresponding to $Mo_2C$ (COD-5910009) [21] and the other set (2θ of around 44, 51, and 76°) contributed by the respective face-centered cubic (FCC) alloy components, confirming the successful formation of $Mo_2C$/alloy heterostructured catalysts. Notably, no diffraction peaks associated with iron/nickel carbides are observed. This can be attributed to the much stronger binding affinity of Mo toward carbon as compared to those of Ni and Fe, making Mo the most favorable element among the three for carbide formation [22]. The intermediate precursors were reduced to form corresponding metals upon thermal reduction at 600°C and part of the Mo reacts with carbon of the carbon source, here MCNT, for formation of $Mo_2C$, whereas the rest of the Mo dissolves into the FCC Ni/Ni-Fe matrices to form NiMo/FeNiMo alloys. Note that the presence of Ni stabilizes the FCC structure even though the thermodynamically stable phases of Mo and Fe at low temperatures are both body-centered cubic (BCC) phase. The phase fractions of $Mo_2C$ and FCC-alloy in the two heterostructured catalysts were estimated with Rietveld refinement of the XRD spectra to be 36% $Mo_2C$ and 64% FCC-NiMo for $Mo_2C$/NiMo and 29% $Mo_2C$ and 71% FCC-FeNiMo for $Mo_2C$/FeNiMo. As for NiMo and FeNiMo, typical diffraction peaks of the FCC phase are observed, with no impurity peaks present, indicating the pure FCC nature of the two alloys. For $Mo_2C$, in addition to the characteristic diffraction peaks of $Mo_2C$, extra diffraction peaks associated with graphitic carbon and FCC Ni are also observed. The diffraction peak of graphitic carbons at 2θ of around 26° comes from the residual carbon source, MCNT, and those of Ni at 2θ of around 45, 52, and 77° is contributed by the Ni contamination from the NF substrate when scraping $Mo_2C$ from the NF substrate at the sample preparation step. The metallic compositions of the five sample catalysts, determined with ICP-OES, are summarized in **Table S1** for comparison. Evidently, all alloy components are Ni based, ensuring their FCC crystalline phases.

**Figure 1b** and **1c** show the morphologies of $Mo_2C$/NiMo and $Mo_2C$/FeNiMo, respectively, with locally enlarged images shown in the insets for close examination. The morphologies of the control samples, $Mo_2C$,

View Article Online
DOI: 10.1039/D6TA02888H

NiMo, and FeNiMo are displayed in **Figure S1** for comparison. Notably, the characteristic dimension of $Mo_2C$/FeNiMo (inset of **Figure 1c**) is appreciably smaller than that of $Mo_2C$/NiMo (inset of **Figure 1b**). Under similar synthetic conditions, FeNiMo alloys typically exhibit smaller product sizes than NiMo alloys because of enhanced lattice distortion and suppressed grain growth in the presence of an extra element, here Fe. If compared with the control samples, the two alloy control samples, NiMo (**Figure S1f**) and FeNiMo (**Figure S1i**), exhibit even larger characteristic dimensions than the two heterostructured catalysts. In the presence of $Mo_2C$, a material of extremely high melting point (~2690 $^oC$), the sintering of the alloys is obstructed, leading to smaller product sizes. The two heterostructured catalysts thus possess porous structures of finer structural features, resulting in higher surface areas to expose abundant accessible active sites for catalysis of the involved electrochemical reactions and consequently enhancing electrocatalytic performances.

In addition to SEM imaging, HRTEM and STEM-EDS were conducted to investigate the detailed crystalline structure and elemental distributions of the sample catalysts. **Figure 1d-1f** present the HRTEM images and elemental distributions of $Mo_2C$/NiMo. As shown in **Figure 1e**, $Mo_2C$ domain is identified from the (112) and (101) planes, showing interlayer distances of 0.13 and 0.23 nm, respectively. The angle contained between the two planes is measured to be 31.5$^o$, in reasonable agreement with the theoretical value of 30°. As for the NiMo alloy domain, the interlayer distances of 0.21 and 0.18 nm are determined for the (211) and (130) planes, respectively, which contain an angle of 52°, in reasonable agreement with the theoretical value of 50°. Furthermore, STEM-EDS elemental mapping confirms that Ni, Mo, and C are uniformly distributed in the catalyst. Formation of the $Mo_2C$/NiMo heterostructure is thus confirmed. **Figure 1g-1i** show the HRTEM images and STEM-EDS elemental mapping of $Mo_2C$/FeNiMo. As shown in **Figure 1h**, the $Mo_2C$ domain exhibits the same lattice planes as observed in $Mo_2C$/NiMo, namely (112) and (101). For the FeNiMo alloy domain, the (130) and (420) planes are identified with the interlayer distances of 0.18 and 0.13 nm, respectively. The angle contained by the (130) and (420) planes is measured to be 46.7°, in reasonable agreement with the theoretical value of 45$^o$. In addition, STEM-EDS elemental mapping (**Figure 1i**) reveals uniform distributions of Fe, Ni, Mo, and C in the catalyst. These results confirm that $Mo_2C$/FeNiMo contains both $Mo_2C$ and FeNiMo, thereby verifying the successful formation of the heterostructured catalyst.

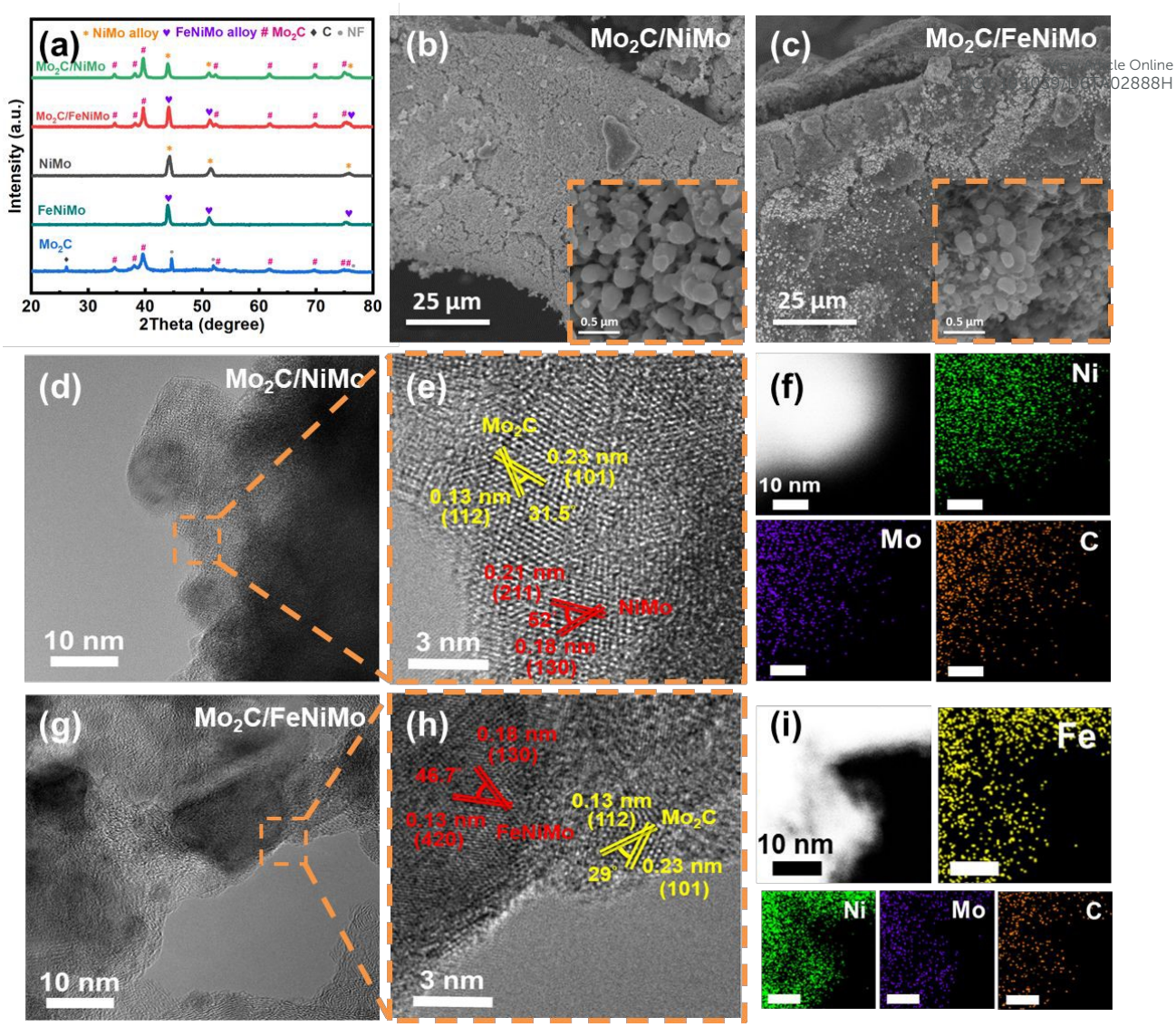


**Figure 1.** (a) XRD patterns of $Mo_2C$/NiMo, $Mo_2C$/FeNiMo, NiMo, FeNiMo, and $Mo_2C$. (b, c) SEM images of $Mo_2C$/NiMo and $Mo_2C$/FeNiMo, respectively, with insets showing locally enlarged images. HR-TEM images, locally enlarged images showing lattice fringes, and corresponding STEM-EDS elemental mapping for (d-f) $Mo_2C$/NiMo and (g-i) $Mo_2C$/FeNiMo.

The five sample catalysts were further characterized with XAS to examine the local structures and chemical states of their constituent elements. They were compared in two groups, the HER group containing $Mo_2C$/NiMo and its control samples, $Mo_2C$ and NiMo, and the OER group containing $Mo_2C$/FeNiMo and its control samples, $Mo_2C$ and FeNiMo. For the HER group, the X-ray absorption near-edge structure (XANES) spectra of Ni K-edge and Mo K-edge are shown in **Figure 2a** and **2b**, respectively for comparison. Evidently, the absorption edge of Ni K-edge of $Mo_2C$/NiMo shifts to a higher energy as compared with that of the control sample NiMo. This positive shift indicates a decrease in electron density around Ni, suggesting that Ni becomes more electron-deficient in the presence of $Mo_2C$. This can be attributed to the strong electronic interactions at the $Mo_2C$/NiMo interface, where charge transfer from Ni to the electron-withdrawing $Mo_2C$ occurs. Note that carbon in $Mo_2C$ polarizes the Mo-C bonds, rendering the Mo centers

View Article Online
DOI: 10.1039/D6TA02888H





electronically deficient, thereby promoting electron donation from Ni. **Figure 2b** shows the XANES spectra of Mo K-edge of $Mo_2C$/NiMo, NiMo, and $Mo_2C$. Here, Mo exists in a metallic state in NiMo and in a low-valent, electron-deficient state in $Mo_2C$. Consequently, $Mo_2C$/NiMo, which contains Mo in both chemical states, exhibits an absorption edge positioning between those of NiMo and $Mo_2C$.

**Figure 2c** and **2d** show the corresponding Fourier-transformed extended X-ray absorption fine structure (FT-EXAFS) spectra of Ni and Mo K-edges, respectively. The first coordination shell of Ni K-edge is located at around 2.2 Å, accounting for the coordination of Ni with its nearest neighboring metal atoms, Ni and Mo, denoted as Ni-M [23, 24], for both $Mo_2C$/NiMo and NiMo. As for the Mo K-edge, the FT-EXAFS spectrum for NiMo is distinctly different from those of $Mo_2C$/NiMo and $Mo_2C$. For NiMo, the first coordination shell is located at around 2.2 Å, accounting for the coordination of Mo with its nearest neighboring metal atoms, Mo and Ni, denoted as Mo-M [23,24]. As for $Mo_2C$/NiMo and $Mo_2C$, the first coordination shell is located at around 1.7 and 1.6 Å, respectively, accounting for the Mo-C bonds in $Mo_2C$. Note that the Mo-C bond in $Mo_2C$/NiMo is slightly longer than that in $Mo_2C$. For $Mo_2C$/NiMo, it is inferred from **Figure 2a** that electrons flow from Ni to $Mo_2C$ in $Mo_2C$/NiMo, rendering electron-rich Mo in $Mo_2C$ of $Mo_2C$/NiMo as compared with Mo in plain $Mo_2C$. The enhanced electron-electron repulsion between electron-rich Mo and electron-rich C thus lengthens the Mo-C bond. The second coordination shell is located at around 2.7 Å, attributable mainly to the Mo-Mo bond in $Mo_2C$ [25, 26], with a low-intensity shoulder located at 2.2 Å accounting for the Mo-M (M=Ni, Mo) bond in NiMo.

For the OER group, the characteristic features of the XANES and FT-EXAFS spectra are similar to those of the HER group. The XANES spectra of Fe and Ni K-edges are displayed in **Figure 2e** and **2f**, respectively. The absorption edges of Fe and Ni K-edges of $Mo_2C$/FeNiMo both shift to higher energies as compared with those of FeNiMo, indicating electron transfer from Fe and Ni to $Mo_2C$. Figure 2**g**), the absorption edge of $Mo_2C$/FeNiMo also positions between those of FeNiMo and $Mo_2C$ because of the mixed chemical states of Mo in the composite. For the corresponding FT-EXAFS spectra, the first coordination shells of Fe and Ni K-edges (**Figures 2h** and **2i**) are both located at around 2.2 Å, accounting for the coordination of Fe and Ni with their nearest neighboring metal atoms, Fe, Ni, and Mo, denoted as Fe-M and Ni-M [23, 24], for both $Mo_2C$/FeNiMo and FeNiMo. As for the Mo K-edge (**Figure 2j**), the FT-EXAFS spectrum for FeNiMo is distinctly different from those of $Mo_2C$/FeNiMo and $Mo_2C$. For FeNiMo, the first coordination shell is located at around 2.2 Å, accounting for the coordination of Mo with its nearest neighboring metal atoms, Mo, Fe, and Ni, denoted as Mo-M [23,24]. As for $Mo_2C$/FeNiMo and $Mo_2C$, the first coordination shell is located at around 1.7 and 1.6 Å, respectively, similar to the situation observed for $Mo_2C$/NiMo (**Figure 2d**), accounting for the Mo-C bonds in $Mo_2C$. The second coordination shell is located at around 2.7 Å, attributable mainly to the Mo-Mo bond in $Mo_2C$ [25, 26], with a low-intensity shoulder located at 2.2 Å accounting for the Mo-Fe/Ni bond in FeNiMo [25,26]. Overall, the XAS measurements indicate that both

$Mo_2C$/NiMo and $Mo_2C$/FeNiMo possess the characteristic features of the carbide/alloy heterostructure, thereby further confirming the successful formation of the carbide/alloy heterostructured catalysts.

View Article Online
DOI: 10.1039/D6TA02888H



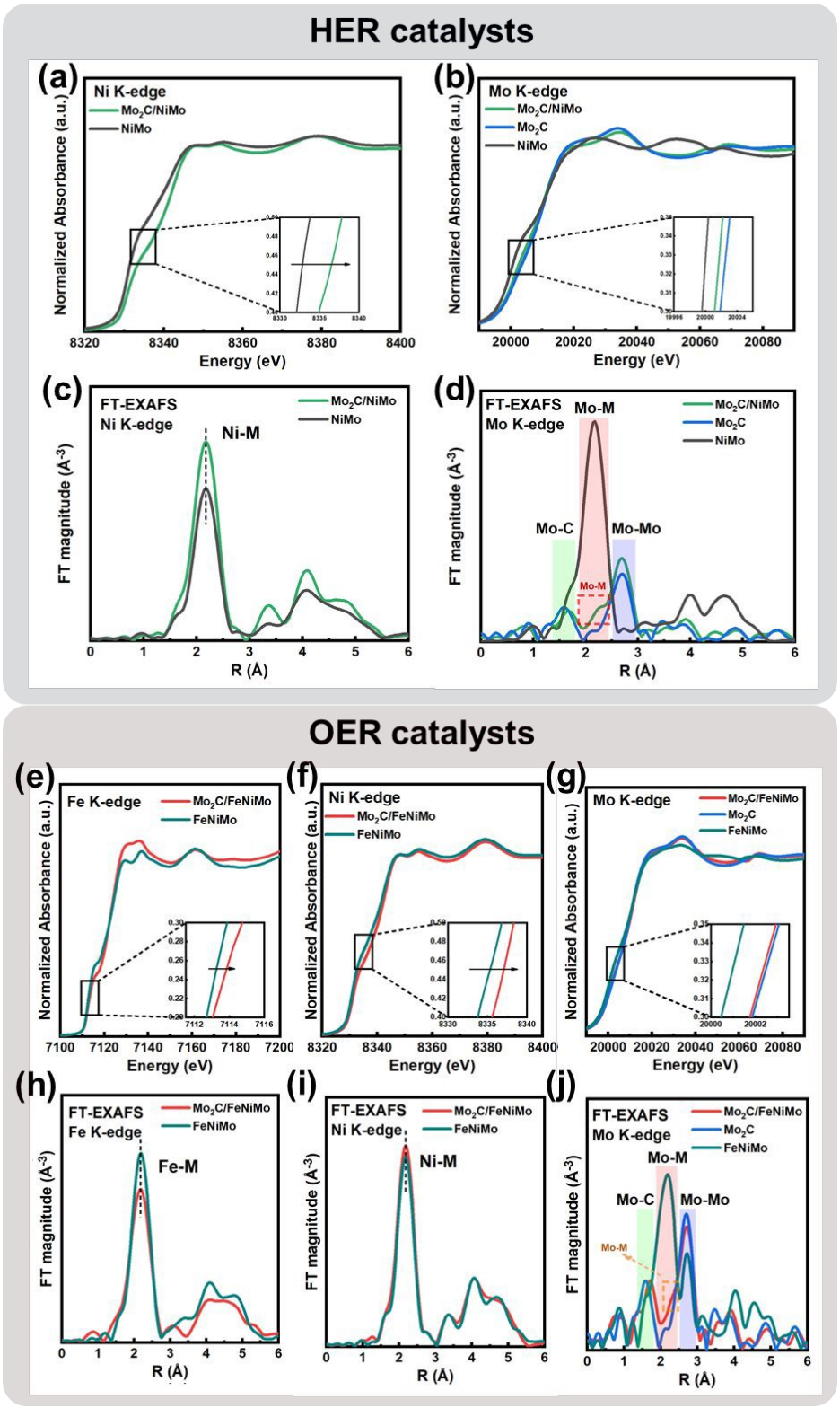


**Figure 2.** (a,b) XANES and (c,d) $k^2$-weighted FT-EXAFS spectra of Ni and Mo K-edges of $Mo_2C$/NiMo, $Mo_2C$, and NiMo. (e,f,g) XANES and (h,i,j) $k^2$-weighted FT-EXAFS spectra of Fe, Ni, and Mo K-edges of $Mo_2C$/FeNiMo, $Mo_2C$, and FeNiMo. Insets in XANES spectra show locally enlarged absorption edges.

### 3.2. Surface Characterizations

High-resolution X-ray photoelectron spectroscopy (HRXPS) was conducted to further investigate the surface chemical states and electronic structure of the sample catalysts. **Figure 3a-3c** display the HRXPS spectra of Ni 2p, C 1s, and Mo 3d, respectively for $Mo_2C$/NiMo, along with those of the two control samples, $Mo_2C$ and NiMo. These spectra provide insights into the electronic interactions between $Mo_2C$ and NiMo within the $Mo_2C$/NiMo heterostructure. The Ni 2p spectra (**Figure 3a**) show the characteristic spin-orbit doublets of Ni $2p_{3/2}$ and Ni $2p_{1/2}$, along with their associated satellite features. The Ni 2p spectra can be deconvoluted into three main constituent peaks: $Ni^0$, $Ni^{2+}$, and the satellite [27, 28]. The presence of $Ni^0$ indicates the existence of metallic nickel in the samples, whereas the $Ni^{2+}$ signal originates from surface oxidation of the samples upon exposure to ambient atmosphere. The detailed characteristic binding energies of Ni 2p are summarized in **Table S2** for comparison. By comparison, the Ni 2p peaks of $Mo_2C$/NiMo exhibit a slight positive shift in binding energies as compared with those of NiMo, consistent with the relevant finding derived from the XANES spectra of Ni K-edge (**Figure 2a**), confirming electron transfer from Ni to $Mo_2C$ in $Mo_2C$/NiMo. In the C 1s spectra (**Figure 3b**), four characteristic peaks can be identified from the broad envelop spanning from 283 to 291 eV through deconvolution. The four peaks are contributed by the Mo-C, C-C/C-H, C-O, and C=O bonds [29-31] in order of increasing binding energies (**Table S3**). The presence of the carbidic carbon bond, Mo-C, confirms the formation of $Mo_2C$, whereas the C-C/C-H, C-O, and C=O peaks are from the organic surface contaminants deposited upon exposure of the sample to ambient atmosphere. The binding energies of the Mo-C peaks of $Mo_2C$/NiMo and $Mo_2C$ are the same (**Table S3**), suggesting that the chemical environment and electronic state of the carbidic carbon remain essentially unchanged upon integration of $Mo_2C$ with NiMo alloy for formation of the $Mo_2C$/NiMo heterostructure. This outcome can be attributed to the covalent nature of the Mo-C bonding, in which electrons are more localized compared to metallic bonding, thus limiting their susceptibilities to neighboring electronic perturbations. Moreover, the alloy phase does not directly bond with the carbon in $Mo_2C$ of $Mo_2C$/NiMo, making it less likely to induce significant changes in the electron density of the carbon. **Figure 3c** shows the HRXPS spectra of Mo 3d, which can be deconvoluted into four constituent components, including $Mo^0$, $Mo^{2+}$, $Mo^{4+}$, and $Mo^{6+}$ in increasing binding energies [32, 33] (**Table S4**). Besides the dominant $Mo^{2+}$ from $Mo_2C$ and metallic Mo from NiMo, because of the high susceptibility (low reduction potential) of Mo to oxidation, higher valence species, $Mo^{4+}$ and $Mo^{6+}$, form from surface oxidation of the sample upon exposure to ambient atmosphere, are also observed. It is evident from **Table S4** that the Mo 3d peaks in $Mo_2C$/NiMo exhibit a slight negative shift as compared with those of $Mo_2C$ and NiMo, suggesting that Mo in $Mo_2C$ of $Mo_2C$/NiMo gains electrons from Ni in NiMo of $Mo_2C$/NiMo. Based on the above XPS analyses, it can be concluded that electron transfer occurs from the NiMo domain toward $Mo_2C$ domain within the $Mo_2C$/NiMo heterostructure. Such electron transfer highlights the electronic

synergy between $Mo_2C$ and NiMo, with which the binding strength between the catalyst surface and adsorbed hydrogen ($H_{ads}$) is modulated to facilitate hydrogen desorption and thus $H_2$ evolution, thereby enhancing the HER catalytic activity [34, 35].

View Article Online
DOI: 10.1039/D6TA02888H

**Figure 3d-3g** show the HRXPS spectra of Fe 2p, Ni 2p, C 1s, and Mo 3d for $Mo_2C$/FeNiMo, together with those of the two control samples, $Mo_2C$ and FeNiMo. The HRXPS spectra of Fe 2p (**Figure 3d**) reveal the presence of three chemical states of Fe, namely metallic Fe ($Fe^0$), $Fe^{2+}$, and $Fe^{3+}$, along with the satellite peaks [36, 37] in order of increasing binding energies (**Table S5**) for both $Mo_2C$/FeNiMo and FeNiMo. The showing of $Fe^{2+}$ and $Fe^{3+}$ again is attributed to the surface oxidation of the samples. The Fe 2p peaks of $Mo_2C$/FeNiMo exhibit a slight positive shift in binding energies as compared with those of FeNiMo, consistent with the relevant finding derived from the XANES spectra of Fe K-edge (**Figure 1e**), confirming electron transfer from Fe to $Mo_2C$ in $Mo_2C$/FeNiMo. The Ni 2p spectra (**Figure 3e**) exhibits characteristic signals of $Ni^0$ and $Ni^{2+}$, along with the satellite peaks [27, 28], in order of increasing binding energies (**Table S6**) for both $Mo_2C$/FeNiMo and FeNiMo. Similarly, the Ni 2p peaks of $Mo_2C$/FeNiMo exhibit a slight positive shift in binding energies as compared with those of FeNiMo, consistent with the relevant finding derived from the XANES spectra of Ni K-edge (**Figure 2f**), confirming electron transfer from Ni to $Mo_2C$ in $Mo_2C$/FeNiMo. The C 1s spectrum (**Figure 3f**) can be deconvoluted into four main peaks, corresponding to Mo-C, C-C, C-O, and C=O bonds, in order of increasing binding energies (**Table S7**). Similar to the case of $Mo_2C$/NiMo, no peak position shifts are observed for the Mo-C bond of $Mo_2C$/FeNiMo, indicating that the electronic environment of the carbidic carbon remains unchanged in $Mo_2C$/FeNiMo as compared to that in $Mo_2C$. This observation suggests that the covalent nature of the Mo-C bonding restricts electron redistribution, and that the integration of $Mo_2C$ with FeNiMo does not alter the electronic states of the carbon in $Mo_2C$. **Figure 3g** shows the HRXPS spectra of Mo 3d, which are composed of four characteristic peaks, namely metallic Mo ($Mo^0$), $Mo^{2+}$, $Mo^{4+}$, and $Mo^{6+}$, in order of increasing binding energies (**Table S8**). The Mo 3d peaks in $Mo_2C$/FeNiMo exhibit a slight negative shift as compared with those of $Mo_2C$ and FeNiMo, suggesting that Mo in $Mo_2C$ of $Mo_2C$/FeNiMo gains electrons from Fe and Ni in FeNiMo of $Mo_2C$/FeNiMo. Based on the above analyses, a finding similar to that observed in $Mo_2C$/NiMo is concluded. Within the $Mo_2C$/FeNiMo heterostructure, Fe and Ni of FeNiMo transfer electrons to $Mo_2C$, resulting in positive shifts of the characteristic binding energies of Fe and Ni, whereas the characteristic binding energies of Mo decreases accordingly. The presence of abundant $Mo_2C$/FeNiMo heterointerfaces facilitates such electron transfer, which modulates adsorption/desorption energies of oxygen-containing species and optimizes the energy difference of the thermodynamic limiting steps of OER to enhance the OER performance of $Mo_2C$/FeNiMo.

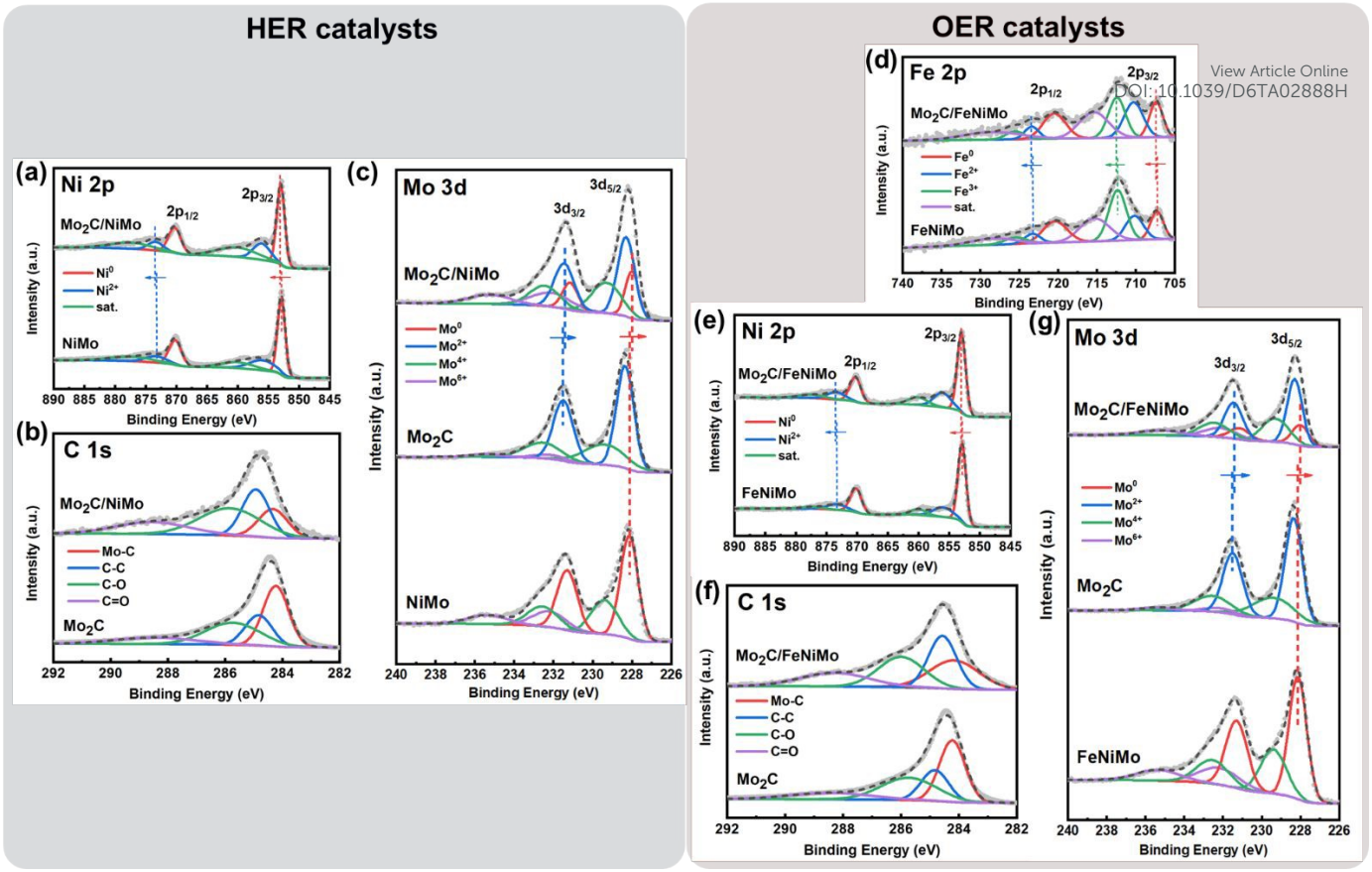


**Figure 3.** HRXPS spectra of (a) Ni 2p, (b) C 1s, and (c) Mo 3d for $Mo_2C$/NiMo, $Mo_2C$, and NiMo. HRXPS spectra of (d) Fe 2p, (e) Ni 2p, (f) C 1s, and (g) Mo 3d for $Mo_2C$/FeNiMo, $Mo_2C$, and FeNiMo.

### 3.3. Electrochemical Characterizations

The electrochemical performances of the five sample catalysts toward catalysis of both HER and OER were characterized with a three-electrode system in 1.0 M KOH. To ensure the accuracy of potential measurements, the Hg/HgO reference electrode was calibrated before use as illustrated in **Figure S2**. Linear sweep voltammetry and electrochemical impedance spectroscopy were conducted for all sample catalysts, with commercial noble metal based catalysts as benchmarks for comparison, Pt/C for HER and $IrO_2$ for OER.

Evident from the LSV polarization curves (**Figure 4a**), the catalytic efficiency of the sample catalysts toward HER follows the trend: $Mo_2C$/NiMo > $Mo_2C$ > $Mo_2C$/FeNiMo > NiMo > FeNiMo. Among the five sample catalysts, the $Mo_2C$/NiMo heterostructure exhibits the best catalytic performance toward HER, achieving current densities of 10 and 500 mA $cm^{-2}$ at overpotentials of 37 ($\eta_{10}$) and 169 mV ($\eta_{500}$), respectively and a mass activity of 0.63 A $g^{-1}$ at η of 50 mV. As a comparison, the corresponding single component catalysts, $Mo_2C$ and NiMo, exhibit lower HER catalytic efficiency as compared to that of $Mo_2C$/NiMo, clearly demonstrating the positive synergy between $Mo_2C$ and NiMo to boost the HER catalytic efficiency of $Mo_2C$/NiMo. Interestingly, inclusion of Fe in $Mo_2C$/NiMo leads to reduction in HER activities of $Mo_2C$/NiMo, even inferior to the plain $Mo_2C$. This phenomenon can be attributed to the strong

View Article Online
DOI: 10.1039/D6TA02888H



oxophilicity of Fe, giving excessive OH adsorption and thus impeding H adsorption/desorption. $Mo_2C$/NiMo also shows the lowest Tafel slope of 74.6 mV $dec^{-1}$ (**Figure 4b**), indicating its relatively fast HER kinetics among the three sample catalysts. With a Tafel slope falling in between 120 and 40 mV $dec^{-1}$, it implies comparable Volmer (120 mV $dec^{-1}$, electrochemical hydrogen adsorption: $* + H_2O + e^- \rightarrow H^* + OH^-$) and Heyrovsky steps (40 mV $dec^{-1}$, electrochemical hydrogen desorption: $H^* + H_2O + e^- \rightarrow H_2 + OH^- + *$), both involving water dissociation, as the thermodynamic rate-determining step of the HER process [38]. As for the catalytic performances toward catalysis of OER, the OER catalytic efficiency follows the trend: $Mo_2C$/FeNiMo > FeNiMo > $Mo_2C$/NiMo ≈ $Mo_2C$ > NiMo (**Figure 4b**). Again, the results clearly demonstrate the positive synergy between $Mo_2C$ and FeNiMo to boost the OER catalytic efficiency of $Mo_2C$/FeNiMo. The $Mo_2C$/FeNiMo heterostructure exhibits the best OER performance, achieving current densities of 10 and 500 mA $cm^{-2}$ at overpotentials of 218 ($\eta_{10}$) and 303 mV ($\eta_{500}$), respectively (**Figure 4d**) and a mass activity of 15.9 A $g^{-1}$ at η of 300 mV. Here, inclusion of Fe to $Mo_2$/NiMo boosts the OER activities of $Mo_2C$/NiMo, even superior to the plain FeNiMo. This phenomenon can be attributed again to the strong oxophilicity of Fe, stabilizing the OER-active oxygenated intermediates and accelerating the high-valence redox transitions required for high OER activities. $Mo_2C$/FeNiMo also shows the lowest Tafel slope of 32.7 mV $dec^{-1}$ (**Figure 4e**), highlighting its fast OER kinetics. The overpotentials and Tafel slopes of all characterized samples toward catalysis of HER and OER are summarized in **Figure 4g** for comparison. Evidently, for overall water electrolysis, the coupling of $Mo_2C$/NiMo and $Mo_2C$/FeNiMo as the cathode and anode catalysts, respectively gives a lowest total overpotential of 472 mV at 500 mA $cm^{-2}$, a commercially relevant operation current density, largely outperforming 610 mV achieved by the Pt/C//$IrO_2$ couple. One concludes from the above observations that the positive synergy between the single component catalysts, $Mo_2C$ and NiMo/FeNiMo, enhances the catalytic efficiency of the resulting heterostructured catalysts toward both HER and OER.

EIS measurements were conducted at -0.2 and 1.53 V (vs. RHE) (**Figure 4c** and **4f**) to further examine the reaction kinetics toward HER and OER, respectively. Nyquist plots were fitted with an equivalent circuit model (insets of **Figure 4c** and **4f** for HER and OER, respectively) [39] to determine the values of charge transfer resistances ($R_{ct}$). The fitting results are summarized in **Tables S9** and **S10** for HER and OER, respectively for comparison. The lowest $R_{ct}$ values for HER and OER are achieved by $Mo_2C$/NiMo and $Mo_2C$/FeNiMo, respectively, in line with the outcomes of overpotentials and Tafel slopes. This highlights that heterostructured catalysts, relative to their single component counterparts, offer superior electron transfer efficiency at the catalyst-electrolyte interface and thus higher catalytic efficiency.

Double-layer capacitances ($C_{dl}$'s), in direct proportionality to electrochemical active surface areas (ECSA's), were determined from cyclic voltammograms recorded within non-Faradaic potential windows at increasing scan rates to serve as a quantitative measure of the quantity of exposed active sites for

View Article Online
DOI: 10.1039/D6TA02888H

assessment of the intrinsic catalytic efficiency of the sample catalysts. The $C_{dl}$'s of the sample catalysts are shown in **Figure S3a**, with the corresponding plots of scan rates versus current density differences presented in **Figures S3b-S3f**. The magnitudes of the $C_{dl}$'s follow the decreasing order of $Mo_2C$/FeNiMo (161.7 mF $cm^{-2}$) > $Mo_2C$ (155.6) > $Mo_2C$/NiMo (140.2) > FeNiMo (9.9) > NiMo (8.2). It is evident that the carbide containing samples exhibit significantly higher $C_{dl}$'s as compared with those achieved by the alloy samples without the presence of carbides. Carbonaceous materials are known to possess good electrical conductivities and large specific surface areas, which facilitate ion adsorption/desorption for high $C_{dl}$'s. From the comparison of the $C_{dl}$'s of the five sample catalysts, it is evident that $Mo_2C$ is the major contributor to the $C_{dl}$'s of the two heterostructured catalysts, with the alloys contributing only very limited $C_{dl}$'s.

The catalytic efficiency of a catalyst is mainly determined by the quantity and quality of the active sites of the catalyst. The effect of the quantity of the active sites may be excluded through normalization of the LSV curve with $C_{dl}$ to give a qualitative measure of the intrinsic activity of the active sites of the catalyst, provided that the main contributor of the $C_{dl}$ of the catalyst is also the main contributor of the catalytic efficiency of the catalyst. For HER, the catalytic efficiency of $Mo_2C$ is close to that of $Mo_2C$/NiMo (**Figure 4a**), indicating that $Mo_2C$ is the main contributor of the catalytic efficiency of $Mo_2C$/NiMo. Nevertheless, for OER, the catalytic efficiency of FeNiMo, instead of $Mo_2C$, is close to that of $Mo_2C$/FeNiMo (**Figure 4d**), indicating that FeNiMo, instead of $Mo_2C$, is the main contributor of the catalytic efficiency of $Mo_2C$/FeNiMo. Recall that $Mo_2C$ is the main contributor to the $C_{dl}$'s of both $Mo_2C$/NiMo and $Mo_2C$/FeNiMo. Consequently, the approach of $C_{dl}$-normalization for intrinsic activity assessment would give reliable results for HER catalyzed by $Mo_2C$/NiMo, but may not work properly for OER catalyzed by $Mo_2C$/FeNiMo. The $C_{dl}$-normalized LSV curves are presented in **Figure S4a** and **S4b for** HER and OER, respectively for comparison. From **Figure S4a**, it is evident that $Mo_2C$/NiMo exhibits the best intrinsic activity, outperforming its single component counterparts, $Mo_2C$ and NiMo. As for OER, **Figure S4b** shows that FeNiMo possesses the highest intrinsic activity, even higher than that of $Mo_2C$/FeNiMo. Here, $Mo_2C$, the main contributor to the $C_{dl}$ of $Mo_2C$/FeNiMo, does not exhibit high OER activities, thereby rendering the $C_{dl}$ of $Mo_2C$/FeNiMo an inappropriate parameter to account for the ECSA of $Mo_2C$/FeNiMo and the $C_{dl}$-normalization an inappropriate approach for assessment of the intrinsic OER activity of $Mo_2C$/FeNiMo.

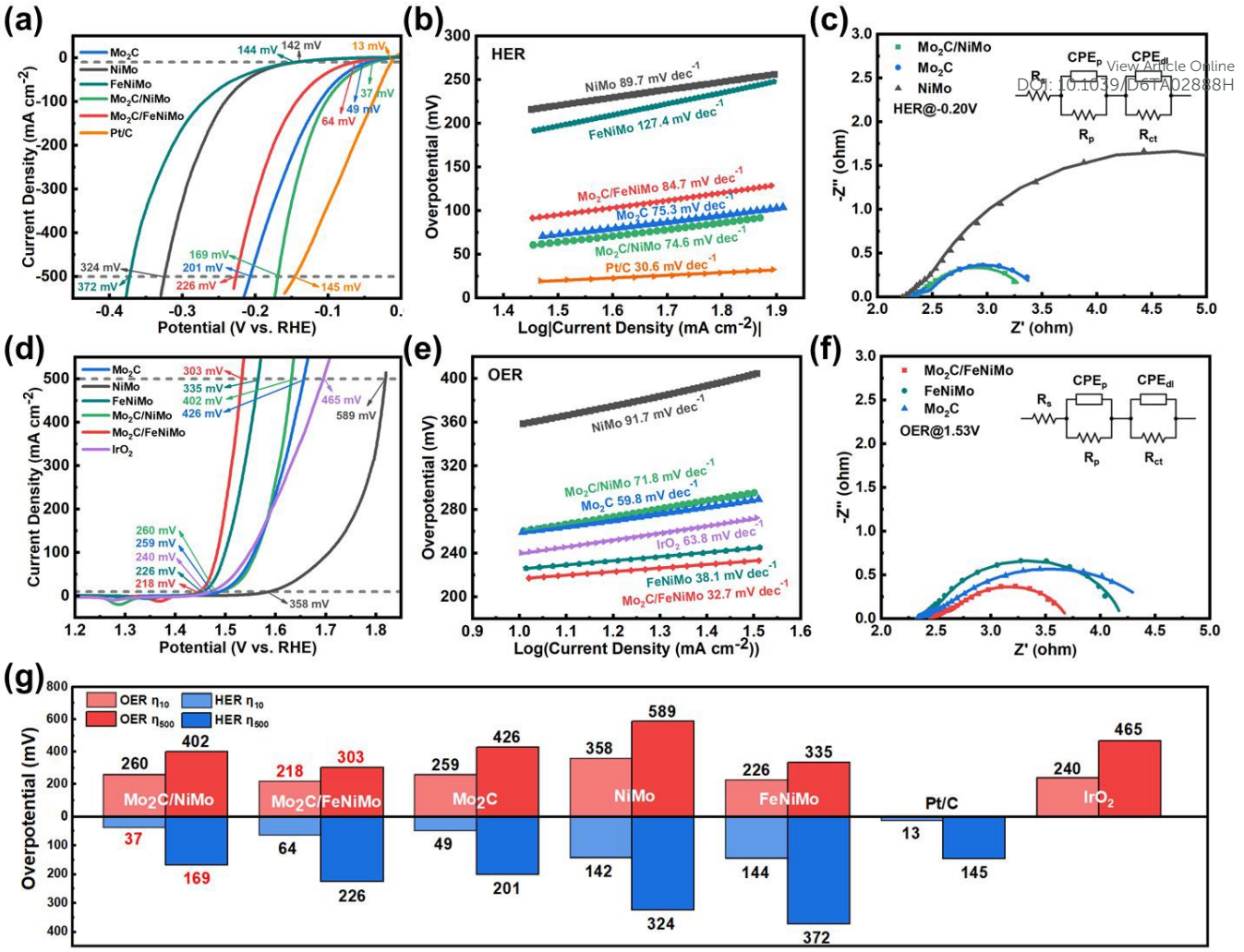


**Figure 4.** Electrochemical characterizations of $Mo_2C$/NiMo, $Mo_2C$/FeNiMo, $Mo_2C$, NiMo, and FeNiMo in 1.0 M KOH: (a) HER LSV curves, (b) HER Tafel plot, (c) Nyquist plot for HER recorded at -0.2 V (vs. RHE), (d) OER LSV curves, (e) OER Tafel plot, (f) Nyquist plot for OER recorded at 1.53 V (vs. RHE), (g) summary of $\eta_{10}$ and $\eta_{500}$ of HER and OER. The Nyquist plot was fitted using an equivalent circuit model consisting of a series system resistance ($R_s$) and two parallel R-CPE branches: one with a porosity related constant phase element ($CPE_p$) and resistance ($R_p$), and the other with a double layer capacitance related constant phase element ($CPE_{dl}$) and charge transfer resistance ($R_{ct}$).

The best performing catalysts for HER, $Mo_2C$/NiMo, and OER, $Mo_2C$/FeNiMo, were coupled as the cathode and anode catalysts for overall water splitting in 1 M KOH. For comparison purpose, cathode//anode couples of $Mo_2C$/NiMo//FeNiMo, $Mo_2C$/NiMo//$Mo_2C$, NiMo//$Mo_2C$/FeNiMo, and $Mo_2C$//$Mo_2C$/FeNiMo were also characterized. **Figure 5a** shows the polarization curves recorded for all sample couples for overall water splitting. Evidently, the $Mo_2C$/NiMo//$Mo_2C$/FeNiMo couple is the champion couple, requiring voltages of only 1.482 (i.e., overpotential of 252 mV) and 1.709 V (i.e., overpotential of 479 mV) to reach current densities of 10 and 500 mA $cm^{-2}$, respectively, outperforming all other couples. Overall, the catalytic efficiency of the five couples for overall water splitting is consistent

with that of the combined corresponding HER and OER half reactions.

The electrochemical performance of the sample catalysts was further characterized in an anion exchange membrane water electrolysis (AEMWE) system. The $Mo_2C$/NiMo@NF and $Mo_2C$/FeNiMo@NF electrodes were used as the cathode and anode, respectively, sandwiching a PiperION anion exchange membrane, to form an AEMWE cell, denoted as $Mo_2C$/NiMo@NF//PiperION//$Mo_2C$/FeNiMo@NF. For comparison purpose, AEMWE cells of $Mo_2C$/NiMo//PiperION//FeNiMo, $Mo_2C$/NiMo//PiperION//$Mo_2C$, NiMo//PiperION//$Mo_2C$/FeNiMo, and $Mo_2C$//PiperION//$Mo_2C$/FeNiMo were also assembled and characterized. All electrochemical characterizations were conducted at 60 °C with a 1.0 M KOH solution circulated through the anode side. The performance of the AEMWE's is shown in **Figure 5b**. Evidently, the $Mo_2C$/NiMo@NF//PiperION//$Mo_2C$/FeNiMo@NF based AEMWE exhibits the best water electrolysis performance, delivering a current density as high as 2.645 A $cm^{-2}$ at a cell voltage of 2.0 V without iR compensation. Overall, the performance trend of the five AEMWE's is consistent with that observed from the corresponding overall water splitting characterizations in aqueous media (**Figure 5a**), confirming that the overall water splitting performance observed in aqueous media are faithfully reflected in the corresponding AEMWE system. **Table S11** summarizes electrochemical performances of the $Mo_2C$/NiMo//PiperION//$Mo_2C$/FeNiMo based AEMWE as compared with those of state-of-the-art non-precious transition metal catalysts based AEMWE's reported in recent years. Evidently, the $Mo_2C$/NiMo//PiperION//$Mo_2C$/FeNiMo based AEMWE stands out strongly.

EIS measurements were conducted on the five AEMWE's at a cell voltage of 1.8 V (**Figure 5c**) to examine internal resistances involved in operations of the AEMWE's. The recorded Nyquist plots are fitted with an equivalent circuit model (inset of **Figure 5c**) to determine the values of high frequency resistance (HFR) and charge transfer resistances ($R_1$ for HER and $R_2$ for OER), as summarized in **Table S12** for comparison. For the HFR, which mainly accounts for ionic resistances of the electrolyte, electronic resistances of the cathode and anode, and contact resistances between components, all five AEMWE's exhibit similar values around 0.021 Ω, implying consistency in cell assembly. As for the two charge transfer resistances, one for the HER at the cathode and the other for the OER at the anode, the values correlate well with the HER/OER catalytic efficiency of the catalysts characterized in 1 M KOH (**Figures 4a** and **4d**), the lower charge transfer resistance for higher catalytic efficiency. Consequently, the $Mo_2C$/NiMo//PiperION//$Mo_2C$/FeNiMo based AEMWE exhibits the lowest $R_1$ of 0.0110 Ω and $R_2$ of 0.0145 Ω. And together with its lowest HFR of 0.019 Ω, the $Mo_2C$/NiMo//PiperION//$Mo_2C$/FeNiMo based AEMWE delivers the highest current density of 2.645 A $cm^{-2}$ at 2.0 V, with the $Mo_2C$ //PiperION//$Mo_2C$/FeNiMo based AEMWE coming next, followed by the $Mo_2C$/NiMo//PiperION// FeNiMo based AEMWE, $Mo_2C$/NiMo//PiperION//$Mo_2C$ based AEMWE, and NiMo//PiperION//FeNiMo based AEMWE in decreasing order.

View Article Online
DOI: 10.1039/D6TA02888H

**Figure 5d** shows the long-term durability of the $Mo_2C$/NiMo@NF//PiperION//$Mo_2C$/FeNiMo@NF based AEMWE, characterized in a chronopotentiometric mode at a commercially relevant constant current density of 0.5 A $cm^{-2}$ for 100 h. The cell exhibits a 6.9 % performance decay, demonstrating its good operational stability and promising potential for green hydrogen production.



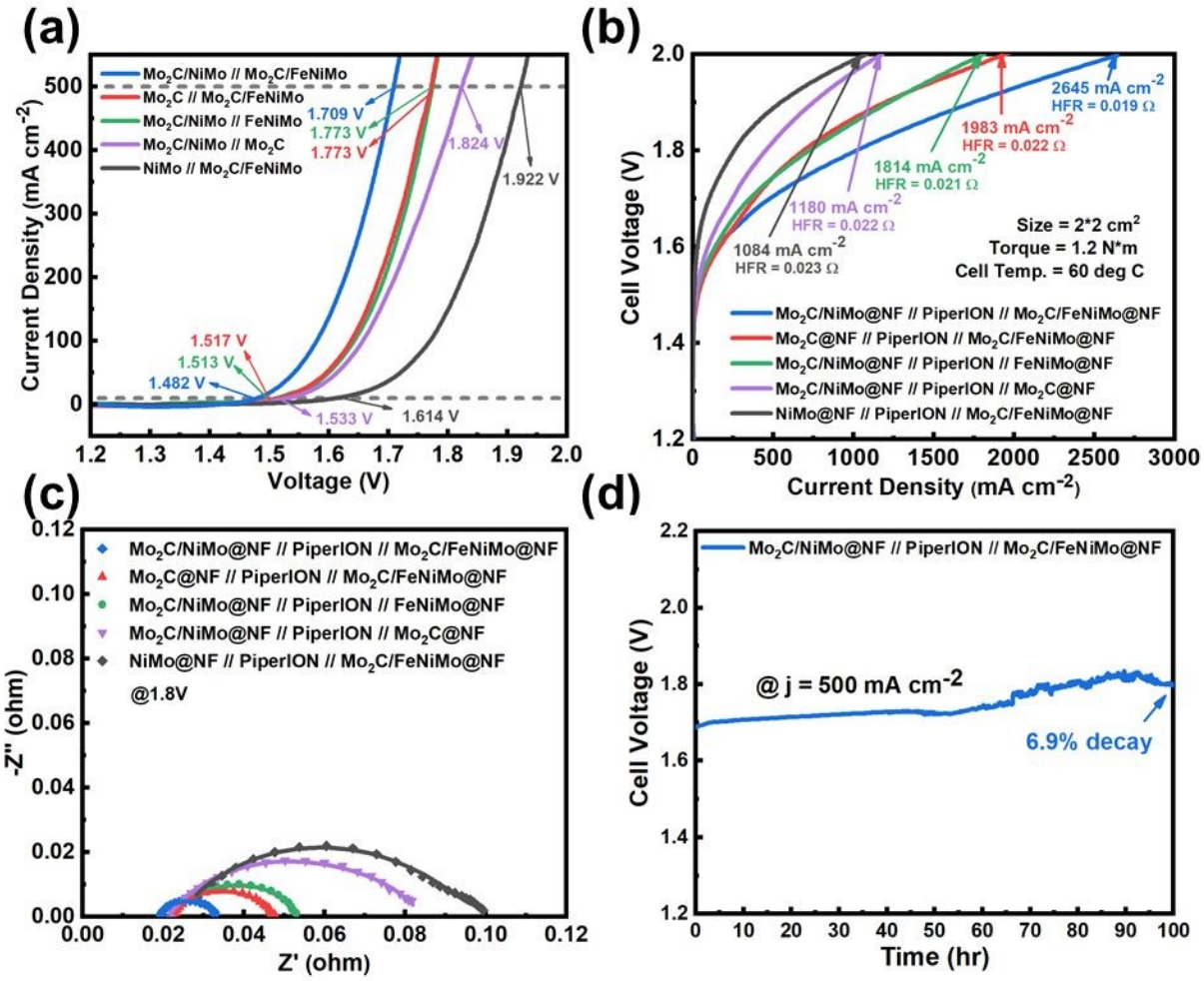


**Figure 5.** LSV curves recorded for overall water splitting of five HER catalyst//OER catalyst couples in 1 M KOH. (b) Polarization curves recorded for five AEMWE's with cathode//PiperION//anode membrane electrode assembly. (c) Nyquist plots recorded at cell voltage of 1.8 V for five AEMWE's. (d) Chronopotentiometric stability test under 0.5 A $cm^{-2}$ for 100 hours for $Mo_2C$/NiMo@NF//PiperION//$Mo_2C$/FeNiMo@NF based AEMWE. For Nyquist plots, all experimental data are plotted in symbols, with fitting results drawn in solid lines. The equivalent circuit model in panel (c) comprises a high frequency resistance ($R_o$), two charge transfer resistances ($R_1$ and $R_2$), and two constant-phase element capacitors ($CPE_1$ and $CPE_2$).

To further examine the electrochemical stability of the HER catalyst, $Mo_2C$/NiMo, and OER catalyst, $Mo_2C$/FeNiMo, chronopotentiometric stability tests were conducted under 0.5 A $cm^{-2}$ for 50 hours in 1 M KOH (**Figures S5a and S5b**). Evidently, both $Mo_2C$/NiMo and $Mo_2C$/FeNiMo outperform their noble metal based benchmark catalysts, Pt/C for HER (0.7 vs. 4.2 % decay) and $IrO_2$ for OER (2.4 vs. 4.5 %

decay). The catalysts after the stability tests were collected for XPS (**Figures S6-S7**) characterizations to examine the material stability of the catalysts. The combined surface contents of alloy and $Mo_2C$ on the catalyst are estimated as the ratio of signal peak areas of ($Ni^0$+$Mo^0$+$Mo^{2+}$) versus ($Ni^0$+$Ni^{2+}$+$Mo^0$+$Mo^{2+}$+$Mo^{4+}$+$Mo^{6+}$) for $Mo_2C$/NiMo (**Table S13**) and ($Fe^0$+$Ni^0$+$Mo^0$+$Mo^{2+}$) versus ($Fe^0$+$Fe^{2+}$+$Fe^{3+}$+$Ni^0$+$Ni^{2+}$+$Mo^0$+$Mo^{2+}$+$Mo^{4+}$+$Mo^{6+}$) for $Mo_2C$/FeNiMo (**Table S14**). Comparison of this ratio before and after the stability test reveals the stability of the surface composition of the catalyst against HER and OER operations in corrosive alkaline media. Evidently, even under cathodic bias, corrosive leaching of surface Ni and Mo occurs after prolonged HER operations in alkaline media. As for the prolonged OER operation, surface oxidation for formation of OER-active intermediates, together with corrosive leaching, result in complete removal of zero/low valent species of Fe, Ni, and Mo under anodic bias in alkaline media.

### 3.4. In-situ Analyses

In-situ characterizations, including X-ray absorption spectroscopy and Raman spectroscopy, were conducted to gain insights into the electronic and structural changes of the sample catalysts during HER and OER for mechanistic understanding. In the case of in-situ XAS, variations in XANES and FT-EXAFS spectra are recorded as the applied potential is altered, thereby revealing changes in valence states and local coordination environments of the constituent elements of the sample catalysts. In parallel, in-situ Raman spectroscopy monitors the evolution of vibrational and rotational features under varying applied potentials, offering information on formation of surface active intermediates during HER and OER.

In-situ XAS measurements were conducted on the two best performing catalysts, $Mo_2C$/NiMo for HER and $Mo_2C$/FeNiMo for OER. **Fig. 6a-6b** show the in-situ XANES spectra of Ni and Mo K-edges of $Mo_2C$/NiMo under HER conditions. When the applied potential is reduced from the open circuit potential (OCP) to -0.2 V, the absorption edge of Ni K-edge exhibits no noticeable shifts, whereas that of Mo K-edge shifts toward lower energies. This indicates that the average oxidation state of Ni remains essentially unchanged during HER and the Mo species become more electron-rich under the cathodic bias. When the applied potential returns to OCP, the absorption edge of Mo K-edge shifts back to its original position, indicating the reversibility of the cathodic bias induced electron flow. **Figure S8a** displays the FT-EXAFS spectra of Ni K-edge, showing a prominent first coordination shell located at around 2.2 Å, corresponding to Ni-M coordination (M = Ni or Mo) [40]. Upon application of a reduction potential at -0.2 V, the shell intensity drops slightly as shown in the inset of **Figure S8a**, indicating increased local disorder and thus decreased coordination of Ni. As inferred from the value of Tafel slope of $Mo_2C$/NiMo toward catalysis of HER (**Figure 4b**), the HER proceeds in the Volmer-Heyrovsky route, in which water dissociation is critically involved. Ni is active toward catalysis of water dissociation [41], in which dynamic adsorption of $H_2O$ and subsequent formation of Ni*-H and Ni*-OH transiently perturb the local coordination environment of Ni, increasing local disorder and thus reducing the coordination shell intensity. Upon

View Article Online
DOI: 10.1039/D6TA02888H



returning the applied potential back to OCP, the shell intensity resumes its initial state, a result of cease of participation of Ni in catalysis of water dissociation. **Figure S8b** shows the FT-EXAFS spectra of Mo K-edge of $Mo_2C$/NiMo. The pronounced coordination shell located at 1.7 Å corresponds to the Mo-C bond of the $Mo_2C$ phase. Under the HER condition at -0.2 V, the coordination shell intensity is slightly increased. At -0.2 V, Mo becomes electron-rich (**Figure 6b**), which stabilizes and increases ordering of the $Mo_2C$ phase to strengthen Mo–C coordination for the coordination shell intensity increase observed. When the applied potential is returned to OCP, the coordination shell intensity resumes the initial state, a result of the reversible cathodic bias induced electron flow. In the $Mo_2C$/NiMo heterostructured catalyst, H* generated on Ni sites during the Volmer step can migrate to nearby $Mo_2C$ sites in a spillover process. Hydrogen spillover mainly proceeds from sites of stronger hydrogen adsorption, advantageous for H* generation from water dissociation, to sites of weaker hydrogen adsorption [42]. Here, the hydrogen adsorption energies of Ni, around -2.6 eV [43-44], is much lower than that of Mo in $Mo_2C$, around -0.8 eV [45-46], facilitating hydrogen spillover from the NiMo phase to the $Mo_2C$ phase. The $Mo_2C$ lattice, being electron-rich and ordered under cathodic bias, stabilizes and accommodates these H* intermediates, preventing excessive surface coverage on Ni. Electron-rich Mo, with an increased d-band occupancy, form moderate Mo–H bonds that retain H* without hindering its eventual combination into $H_2$ for hydrogen desorption, thus facilitating the Heyrovsky step. As an example, the hydrogen adsorption strength on $Mo_2C$ was weakened to give a hydrogen adsorption energy of 0.037 eV, close to the optimal thermoneutral hydrogen adsorption, upon coupling $Mo_2C$ with Ni that donates electrons to $Mo_2C$ to make Mo electron-rich, with which the HER activity of $Mo_2C$ was much improved [47]. This interfacial synergy ensures efficient coupling of water dissociation and $H_2$ desorption during alkaline HER to realize enhanced HER activities of $Mo_2C$/NiMo.

**Fig. 6c-6e** show the in-situ XANES spectra of Fe, Ni, and Mo K-edges of $Mo_2C$/FeNiMo, respectively under OER conditions. As the applied potential increases from OCP to 1.43 V, the absorption edges of Fe, Ni, and Mo K-edges upshift to higher energies, signifying raised valence states of Fe, Ni, and Mo under anodic bias. In alkaline media, OER proceeds as consecutive attack of hydroxide ion on metallic active sites for sequential formation of *OH, *O, and *OOH, followed by desorption of $O_2$ and recovery of the active sites. The adsorption/formation of these oxygen-containing intermediates leads to electron withdrawal from the metallic sites because of the high electronegativity of oxygen. This results in decreases in electron densities around the metal sites, thereby causing upshifts in valence states and thus absorption edges to higher energies. **Figures S9a-S9c** present the corresponding FT-EXAFS spectra of Fe, Ni, and Mo K-edges. Under the OER condition, the Fe-M and Ni-M coordination intensities drop, which can be attributed to the adsorption/formation of the oxygen-containing intermediates. The adsorption/formation of these oxygen-containing intermediates is dynamic and the structure of the formed oxygen-containing intermediates is amorphous, both leading to increased disorders of the local structure around Fe and Ni and

View Article Online
DOI: 10.1039/D6TA02888H

subsequent drops in coordination intensities of the two elements. As for the Mo K-edge spectrum, under the OER condition, the Mo-C coordination shell intensity increases, which can be attributed to partial surface oxidation of $Mo_2C$, converting surface Mo-C bonds to Mo-O bonds. The Mo-C bond is less ordered for electron-deficient Mo under anodic potentials (**Figure 6e**) as compared with the Mo-O bond, which is ordered in $MoO_x$ structure. In addition, O is a heavier atom than C, and offers a stronger backscattering strength to the Mo-O coordination, which overlaps with the Mo-C coordination. The two factors lead to enhanced Mo-C coordination shell intensity. In the $Mo_2C$/FeNiMo heterostructured catalyst, electrons flow from the FeNiMo domain to the $Mo_2C$ domain (**Figure 3g**), leading to more electropositive Fe and Ni for favorable formation of active high-valent intermediates, *OOH, and consequent enhancements in OER activities.

In-situ Raman spectroscopy was conducted to monitor the structural evolution of $Mo_2C$/NiMo and $Mo_2C$/FeNiMo under cathodic and anodic potentials, respectively. **Figure S10a** shows the in-situ Raman spectra of $Mo_2C$/NiMo under HER conditions. Evidently, no significant spectral features emerge during the whole potential course, decreasing from OCP to -0.4 V and back to OCP. In the HER process, no Raman-active intermediates were formed. On the contrary, under OER conditions, $Mo_2C$/FeNiMo exhibits distinct spectral features upon applications of increasing potentials from OCP up to 1.63 V, as shown in **Figure S10b**. Two broad Raman peaks emerge centering around 480 and 560 $cm^{-1}$, attributable to formation of (Ni/Fe)*-OOH intermediates [48]. It has been demonstrated with DFT calculations that Fe-doped NiOOH is thermodynamically favorable, with Fe existing in a low spin state [49]. The low spin state of Fe renders the surface Fe sites highly active for OER. The thermodynamic OER overpotentials computed for Fe-doped and pure NiOOH were 0.42 and 0.77 V, respectively, demonstrating the Fe-doping induced activity enhancement [49]. These two characteristic Raman peaks first emerge at 1.43 V and continuously intensify with increasing anodic potentials. The formation of (Ni/Fe)-OOH intermediates reveals that Ni and Fe are the active sites for catalysis of OER. The presence of $Mo_2C$ in $Mo_2C$/FeNiMo withdraw electrons from FeNiMo, making Ni and Fe more electropositive for more favorable formation of the active oxyhydroxide intermediates and thus enhanced OER activities (**Figure 4d**).

View Article Online
DOI: 10.1039/D6TA02888H



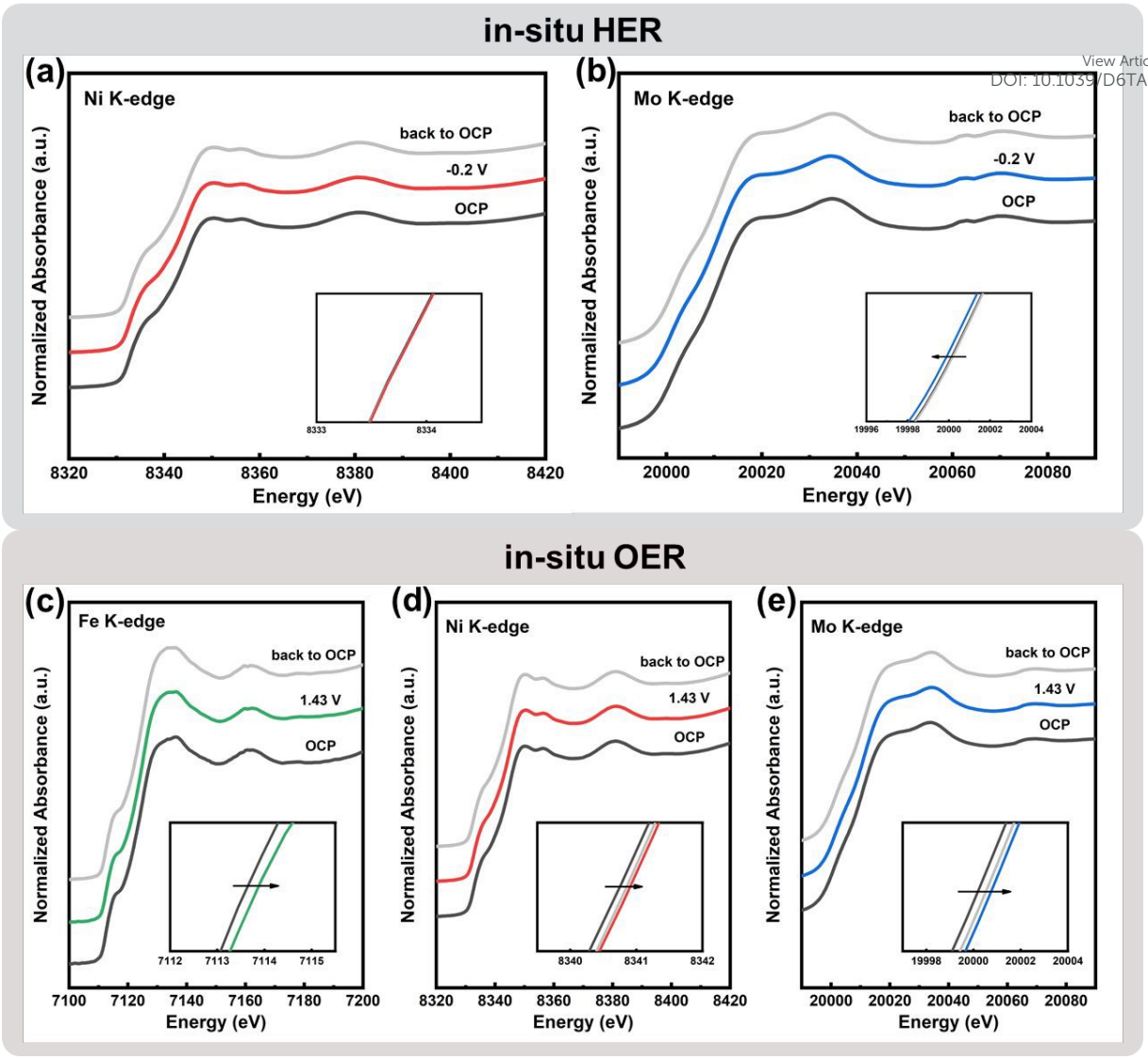


**Fig. 6.** In-situ XANES spectra of $Mo_2C$/NiMo under cathodic condition at (a) Ni K-edge and (b) Mo K-edge. In-situ XANES spectra of $Mo_2C$/FeNiMo under anodic condition at (c) Fe K-edge, (d) Ni K-edge, and (e) Mo K-edge. Cathodic condition: OCP, -0.20 V, and back to OCP. Anodic condition: OCP, 1.43 V, and back to OCP. Insets show corresponding locally enlarged overlaid curves.

## 4. Conclusion

In this study, a simple and fast dip-roast-reduction process was successfully developed to uniformly load carbide/alloy heterostructured catalysts onto Ni foam substrates. For HER and OER, $Mo_2C$/NiMo and $Mo_2C$/FeNiMo heterostructures were specifically designed, respectively, both exhibiting outstanding electrocatalytic efficiency. For HER, $Mo_2C$/NiMo required overpotentials of only 37 and 169 mV to reach current densities of 10 and 500 mA $cm^{-2}$, respectively, with a Tafel slope of 74.6 mV $dec^{-1}$, suggesting a Volmer-Heyrovsky mechanism. For OER, $Mo_2C$/FeNiMo achieved low overpotentials of 218 and 303 mV to deliver current densities of 10 and 500 mA $cm^{-2}$, respectively, with a Tafel slope of only 32.7 mV $dec^{-1}$, indicating fast OER kinetics. XRD, TEM, and XPS analyses confirmed the heterostructured features of the

catalysts, whereas electrochemical measurements confirmed the positive synergy between the carbide and alloy phases for much enhanced activities derived from the heterostructures. When applied in an AEMWE, the MEA constructed with $Mo_2C$/NiMo@NF//PiperION//$Mo_2C$/FeNiMo@NF exhibited remarkable water electrolysis performances, delivering an ultrahigh current density of 2.645 A $cm^{-2}$ at 2.0 V. Moreover, a long-term durability test at 0.5 A $cm^{-2}$ over 50 h showed only a 2.0 % decay, confirming the excellent chemical and mechanical stability and practical applicability of these catalysts under alkaline conditions. The $Mo_2C$/NiMo and $Mo_2C$/FeNiMo heterostructured catalysts, constructed from the combination of carbides and alloys, exhibited excellent catalytic activities by leveraging electronic modulations, optimized adsorptions of hydrogen and oxygenated intermediates, and positive synergy between the constituent phases. These results highlight the great potential of carbide/alloy heterostructured catalysts for practical alkaline water electrolysis applications.

## AUTHOR CONTRIBUTIONS

**Kai-An Lee:** Writing – Original Draft, Conceptualization, Data Curation, Formal Analysis, Investigation, Methodology, Validation, Visualization. **Yu-Chieh Ting:** Data Curation, Formal Analysis. **Chiung-Wen Chang:** Data Curation, Formal Analysis. **Tzu-Hsiang Lin:** Data Curation, Formal Analysis. **Shao-I Chang:** Data Curation, Formal Analysis. **Tsung-Wei Hsueh:** Data Curation, Formal Analysis. **Shih-Yuan Lu:** Writing – review & editing, Conceptualization, Formal Analysis, Investigation, Methodology, Validation, Supervision, Resources, Project administration, Funding acquisition.

## CONFLICT OF INTEREST STATEMENT

The authors declare that they have no known competing financial interests or personal relationships that could have appeared to influence the work reported in this paper.

## DATA AVAILABILITY

The data supporting this article have been included as part of the Supplementary Information. Supplementary information: Scheme S1, Figures S1-S7, and Tables S1-S12. See DOI: https://doi.org/DOI.

## ACKNOWLEDGMENTS

The authors acknowledge the financial support offered by the National Science and Technology Council (NSTC) of Taiwan through grants 113-2218-E-007-013 and 113-2221-E-007-032-MY3. The authors greatly appreciate the beamtime of TPS 44A1 provided by the National Synchrotron Radiation Research Center (NSRRC) of Taiwan, ROC. The authors also appreciate the access to spherical-aberration-corrected

transmission electron microscopy (JEM-ARM200FTH, JEOL Ltd.) and high-resolution X-ray photoelectron spectroscopy (HR-XPS, PHI Quantera II, ULVAC-PHI Inc.) at the Instrumentation Center of the National Tsing Hua University.

View Article Online
DOI: 10.1039/D6TA02888H





## REFERENCES

[1] Yan Y, Xia BY, Zhao B, Wang X, A review on noble-metal-free bifunctional heterogeneous catalysts for overall electrochemical water splitting, *Journal of Materials Chemistry A*, 2016; 4: 17587-603.

[2] Li X, Hao X, Abudula A, Guan G, Nanostructured catalysts for electrochemical water splitting: current state and prospects, *Journal of Materials Chemistry A*, 2016; 4: 11973-2000.

[3] Hu C, Zhang L, Gong J, Recent progress made in the mechanism comprehension and design of electrocatalysts for alkaline water splitting, *Energy Environmetal Science*, 2019; 12: 2620-45.

[4] Li C, Baek JB, The promise of hydrogen production from alkaline anion exchange membrane electrolyzers, *Nano Energy*, 2021; 87: 106162.

[5] Du N, Roy C, Peach R, Turnbull M, Thiele S, Bock C, Anion-exchange membrane water electrolyzers, *Chemical Reviews*, 2022, 13; 11830–11895.

[6] Yang Y, Li P, Zheng X, Sun W, Dou SX, Ma T, Pan, H, Anion-exchange membrane water electrolyzers and fuel cells, *Chemical Society Reviews*, 2022; 51: 9620-93.

[7] Vincent I, Bessarabov D, Low cost hydrogen production by anion exchange membrane electrolysis: A review, *Renewable Sustainable Energy Reviews*, 2018; 81: 1690-704.

[8] Wan L, Xu Z, Xu Q, Pang M, Lin D, Liu J, Wang B, Key components and design strategy of the membrane electrode assembly for alkaline water electrolysis, *Energy Environmental Science*, 2023; 16: 1384-430.

[9] Chang C-W, Ting Y-C, Lee K-A, Chang S-I, Lin K-H, Lu S-Y, Interface engineering effected charge redistribution within high entropy alloy-metal heterostructured catalyst enables high performance anion exchange membrane water electrolysis, *Small*, 2026; 22: e10665.

[10] Yen F-Y, Chang S-I, Ting Y-C, Chang C-W, Lee K-A, Lu S-Y, In-situ selective oxidation created $Cr_2O_3$ assisting CrMnFeCoNi for ultrahigh power density zinc−air batteries, *Energy Materials*, 2025; 5: 500114.

[11] Zhao G, Rui , Dou SX, Sun W, Heterostructures for electrochemical hydrogen evolution reaction: a review, *Advanced Functional Materials*, 2018; 28: 1803291.

[12] Zhang W, Yang L, Li Z, Nie G, Cao X, Fang Z, Wang X, Ramakrishna S, Long Y, Jiao L, Regulating hydrogen/oxygen species adsorption via built-in electric field-driven electron transfer behavior at the heterointerface for efficient water splitting, *Angewandte Chemie International Edition*, 2024; 63:

e202400888.

[13] Wei J, Zhou M, Long A, Xue Y, Liao H, Wei C, Xu ZJ, Heterostructured electrocatalysts for hydrogen evolution reaction under alkaline conditions, *Nano-Micro Letters*, 2018; 10: 75.

[14] Chen P, Ye J, Wang H, Ouyang L, Zhu M, Recent progress of transition metal carbides/nitrides for electrocatalytic water splitting, *Journal of Alloy and Compounds*, 2021; 883: 160833.

[15] Zhong Y, Xia X, Shi F, Zhan J, Tu J, Fan HJ, Transition metal carbides and nitrides in energy storage and conversion, *Advanced Science*, 2016; 3: 1500286.

[16] Lin T-H, Ting Y-C, Chang C-W, Chang S-I, Lee K-A, Hsueh T-W, Lin K-H, Lu S-Y, 3-d element induced charge redistribution of bimetallic η-phase carbides leads to high performance electrocatalysts for highly efficient anion exchange membrane water electrolysis, *Small*, 2025; 21: e11280.

[17] Diao J, Qiu Y, Liu S, Wang W, Chen K, Li H, Yuan W, Qu Y, Guo X, Interfacial engineering of $W_2N$/WC heterostructures derived from solid-state synthesis: a highly efficient trifunctional electrocatalyst for ORR, OER, and HER, *Advanced Materials*, 2020; 32: 1905679.

[18] Zhao Z, Qin F, Kasiraju S, Xie L, Alam MK, Chen S, Wang D, Ren Z, Wang Z, Grabow LC, Bao J, Vertically aligned $MoS_2$/$Mo_2C$ hybrid nanosheets grown on carbon paper for efficient electrocatalytic hydrogen evolution, *ACS Catalysis*, 2017; 7: 7312-7318.

[19] Xu Y, Yang J, Liao T, Ge R, Liu Y, Zhang J, Li Y, Zhu M, Li S, Li W, Bifunctional water splitting enhancement by manipulating Mo-H bonding energy of transition Metal-$Mo_2C$ heterostructure catalysts, *Chemical Engineering Journal*, 2022; 431: 134126.

[20] Yuan S, Xiang L, Li N, Liang T, Wang K, Gao X, Cui M, Zhao L, Modulating electronic structure and mass transfer kinetics via Mo-$Mo_2C$ heterostructure for ampere-level hydrogen evolution, *Advanced Functional Materials*, 2025; 35: 2422514.

[21] Jain A, Ong SP, Hautier G, Chen W, Richards WD, Dacek S, Cholia S, Gunter D, Skinner D, Ceder G, Persson KA, Commentary: The Materials Project: A materials genome approach to accelerating materials innovation, *APL Materials*, 2013; 1: 011002.

[22] Silvearv F, Larsson P, Jones SLT, Ahuja R, Larsson JA, Establishing the most favorable metal-carbon bond strength for carbon nanotube catalysts, *Journal of Materials Chemistry C*, 2015; 3: 3422-7.

[23] Liu W, Yang Y, Chen L, Xu E, Xu J, Hong S, Zhang X, Wei M, Atomically-ordered active sites in NiMo intermetallic compound toward low-pressure hydrodeoxygenation of furfural, *Applied Catalysis B: Environmental*, 2021; 282: 119569.

[24] Huang CL, Lin YG, Chiang C-L, Peng C-K, Senthil Raja D, Hsieh C-T, Chen Y-A, Lu S-Y, Atomic scale synergistic interactions lead to breakthrough catalysts for electrocatalytic water splitting, *Applies Catalysis B: Environmental*, 2023, 320: 122016.

[25] Yang H, Chen X, Hu G, Chen W-T, Bradley SJ, Zhang W, Verma G, Nann T, Jiang D-E, Kruger PE, Wang X, Tian H, Waterhouse GIN, Telfer SG, Ma S, Highly efficient electrocatalytic hydrogen evolution promoted by O–Mo–C interfaces of ultrafine β-$Mo_2C$ nanostructures, *Chemical Science*, 2020; 11: 3523-3530.

[26] Zhang H, Jin H, Yang Y, Sun F, Liu Y, Du X, Zhang S, Song F, Wang J, Wang Y, Jiang Z, Understanding the synergetic interaction within α-MoC/β-$Mo_2C$ heterostructured electrocatalyst, *Journal of Energy Chemistry*, 2019; 35: 66-70.

[27] Qian G, Chen J, Yu T, Liu J, Luo L, Yin S, Three-phase heterojunction NiMo-based nano-needle for water splitting at industrial alkaline condition, *Nano-Micro Letters*, 2022; 14: 20.

[28] Zhang Y, Wang Y, Jia S, Xu H, Zang J, Lu J, Xu X, A hybrid of NiMo-$Mo_2C$/C as non-noble metal electrocatalyst for hydrogen evolution reaction in an acidic solution, *Electrochimica Acta*, 2016; 222: 747-754.

[29] Yang Z, Li M, Chen S, Yang S, Peng F, Liao J, Fang Y, Zhang S, Zhang S, Cocatalyst engineering with robust tunable carbon-encapsulated Mo-rich Mo/$Mo_2C$ heterostructure nanoparticle for efficient photocatalytic hydrogen evolution, *Advanced Functional Materials*, 2023; 33: 2212746.

[30] Attar F, Riaz A, Zhang D, Lu H, Thomsen L, Karuturi S, Advanced NiMoC electrocatalysts precision synthesised at room temperature for efficient hydrogen evolution across pH ranges, *Chemical Engineering Journal*, 2025; 518: 164494.

[31] Zhang Y, Zhen X, Su Z, Guo J, Li J, Liu S, Li X, Ni/MoC@NC as bifunctional electrocatalyst coupled HER and Urea oxidation for energy-efficient hydrogen production, *International Journal of Hydrogen Energy*, 2024; 60: 46-54.

[32] Xu Z, Jin S, Seo MH, Wang X, Hierarchical Ni-$Mo_2C$/N-doped carbon Mott-Schottky array for water electrolysis, *Applied Catalysis B: Environment and Energy*, 2021; 292: 120168.

[33] Ying L, Sun S, Liu W, Zhu H, Zhu Z, Liu A, Yang L, Lu S, Duan F, Yang C, Du M, Heterointerface engineering in bimetal alloy/metal carbide for superior hydrogen evolution reaction, *Renewable Energy*, 2020; 161: 1036-1045.

[34] Li M, Zhu Y, Wang H, Wang C, Pinna N, Lu X, Ni Strongly coupled with $Mo_2C$ encapsulated in nitrogen-doped carbon nanofibers as robust bifunctional catalyst for overall water splitting, *Advanced Energy Materials*, 2019; 9: 1803185.

[35] Sun JH, Liu JN, Chen H, Han X, Wu Y, He J, Han C, Yang G, Shan Y, Strongly coupled $Mo_2C$ and Ni nanoparticles with in-situ formed interfaces encapsulated by porous carbon nanofibers for efficient hydrogen evolution reaction under alkaline conditions, *Journal of Colloid and Interface Science*, 2020; 558: 100-105.

[36] Chen F, Tang M, Zhou J, Zhang H, Su C, Guo S, Fe-based amorphous alloy wire as highly efficient

and stable electrocatalyst for oxygen evolution reaction of water splitting, *Journal of Alloys and Compounds*, 2023; 955: 170253.

View Article Online
DOI: 10.1039/D6TA02888H

[37] Liu H, Xi C, Xin JH, Zhang GL, Zhang SF, Zhang ZJ, Huang Q, Li J, Liu H, Kang J, Free-standing nanoporous NiMnFeMo alloy: an efficient non-precious metal electrocatalyst for water splitting, *Chemical Engineering Journal*, 2021; 404: 126530.

[38] Lasia A, Mechanism and kinetics of the hydrogen evolution reaction, *International Journal of Hydrogen Energy*, 2019; 44: 19484-19518.

[39] Lazanas AC, Prodromidis MI, Electrochemical impedance spectroscopy - a tutorial, *ACS Measurement Science Au*, 2023; 3: 162-193.

[40] Hou M, Zheng L, Zhao D, Tan X, Feng W, Fu J, Wei T, Cao M, Zhang J, Chen C, Microenvironment reconstitution of highly active Ni single atoms on oxygen-incorporated $Mo_2C$ for water splitting, *Nature Communications*, 2024; 15: 1342.

[41] Lei C, Wang Y, Hou Y, Liu P, Yang J, Zhang T, Zhuang X, Chen M, Yang B, Lei L, Yuan C, Qiu M, Feng X, Efficient alkaline hydrogen evolution on atomically dispersed Ni–Nx Species anchored porous carbon with embedded Ni nanoparticles by accelerating water dissociation kinetics, *Energy Environment Science*, 2019; 12: 149.

[42] Sermon PA, Bond GC, Hydrogen spillover, *Catalysis Reviews*, 1974, 8: 211–239.

[43] Weng MH, Chen H-T, Wang Y-C, Ju S-P , Chang J-G, Lin M-C, Kinetics and mechanisms for the adsorption, dissociation, and diffusion of hydrogen in Ni and Ni/YSZ slabs: a DFT study, *Langmuir*, 2012; 28: 5596−5605.

[44] Michaelides A, Hua P, A density functional theory study of $CH_2$ and H adsorption on Ni(111), *Journal of Chemical Physics*, 2000, 112: 6006-6014.

[45] Posada-Pérez S, Viñes F, Valero R, Rodriguez JA, Illas F, Adsorption and dissociation of molecular hydrogen on orthorhombic β-$Mo_2C$ and cubic δ-MoC (001) surfaces, *Surface Science*, 2017, 656: 24–32.

[46] Medford AJ, Vojvodic A, Studt F, Abild-Pedersen F, Nørskov JK, Elementary steps of syngas reactions on $Mo_2C$(001): adsorption thermochemistry and bond dissociation, *Journal of Catalysis*, 2012, 290: 108–117.

[47] Liu Z, He H, Liu Y, Zhang Y, Shi J, Xiong J, Zhou S, Li J, Fan L, Cai W, Soft-template derived Ni/$Mo_2C$ hetero-sheet arrays for large current density hydrogen evolution reaction, *Journal of Colloid and Interface Science*, 2023, 635: 23–31.

[48] Qiu Z, Ma Y, Edvinsson T, In operando Raman investigation of Fe doping influence on catalytic NiO intermediates for enhanced overall water splitting, *Nano Energy*, 2019; 66: 104118.

[49] He Z-D, Tesch R, Eslamibidgoli MJ, Eikerling MH, Kowalski PM, Low-spin state of Fe in Fe-doped NiOOH electrocatalysts, *Nature Communications*, 2023, 14: 3498.

View Article Online
DOI: 10.1039/D6TA02888H

**Data availability statement**

The data supporting this article have been included as part of the Supplementary Information. Supplementary information: Scheme S1, Figures S1-S7, and Tables S1-S12. See DOI: https://doi.org/DOI.